



PAPER • OPEN ACCESS

Scalable fabrication of renal spheroids and nephron-like tubules by bioprinting and controlled self-assembly of epithelial cells

To cite this article: Kevin Tröndle *et al* 2021 *Biofabrication* **13** 035019

View the [article online](#) for updates and enhancements.

You may also like

- [The emergence of 3D bioprinting in organ-on-chip systems](#)
Kirsten Fetah, Peyton Tebon, Marcus J Goudie et al.
- [A nephron-based model of the kidneys for macro-to-micro -particle dosimetry](#)
Robert F Hobbs, Hong Song, David L Huso et al.
- [How to build an epithelial tree](#)
Sarah V Paramore, Katharine Goodwin and Celeste M Nelson

Biofabrication



PAPER

OPEN ACCESS

RECEIVED
26 August 2020

REVISED
9 November 2020

ACCEPTED FOR PUBLICATION
29 January 2021

PUBLISHED
7 April 2021

Original content from
this work may be used
under the terms of the
[Creative Commons
Attribution 4.0 licence](#).

Any further distribution
of this work must
maintain attribution to
the author(s) and the title
of the work, journal
citation and DOI.



Scalable fabrication of renal spheroids and nephron-like tubules by bioprinting and controlled self-assembly of epithelial cells

Kevin Tröndle¹ , Ludovica Rizzo², Roman Pichler³ , Fritz Koch¹, Ahmad Itani¹, Roland Zengerle^{1,4}, Soeren S Lienkamp^{2,3}, Peter Koltay^{1,4} and Stefan Zimmermann¹

¹ Laboratory for MEMS Applications, IMTEK—Department of Microsystems Engineering, University of Freiburg, Georges-Koehler-Allee 103, D-79110 Freiburg, Germany

² Institute of Anatomy and Zurich Center for Integrative Human Physiology (ZIHP), University of Zurich, Zurich, Switzerland

³ Renal Division, Department of Medicine, Faculty of Medicine and Medical Center—University of Freiburg, Freiburg, Germany

⁴ Hahn-Schickard, Georges-Koehler-Allee 103, D-79110 Freiburg, Germany

E-mail: kevin.troendle@imtek.uni-freiburg.de

Keywords: bioprinting, cellular self-assembly, renal cell models, spheroids, nephron tubules, scalable fabrication, fluidic integration
Supplementary material for this article is available [online](#)

Abstract

Scalable fabrication concepts of 3D kidney tissue models are required to enable their application in pharmaceutical high-throughput screenings. Yet the reconstruction of complex tissue structures remains technologically challenging. We present a novel concept reducing the fabrication demands, by using controlled cellular self-assembly to achieve higher tissue complexities from significantly simplified construct designs. We used drop-on-demand bioprinting to fabricate locally confined patterns of renal epithelial cells embedded in a hydrogel matrix. These patterns provide defined local cell densities (cell count variance <11%) with high viability ($92 \pm 2\%$). Based on these patterns, controlled self-assembly leads to the formation of renal spheroids and nephron-like tubules with a predefined size and spatial localization. With this, we fabricated scalable arrays of hollow epithelial spheroids. The spheroid sizes correlated with the initial cell count per unit and could be stepwise adjusted, ranging from $\varnothing = 84, 104, 120\text{--}131\text{ }\mu\text{m}$ in diameter (size variance <9%). Furthermore, we fabricated scalable line-shaped patterns, which self-assembled to hollow cellular tubules ($\varnothing = 105 \pm 22\text{ }\mu\text{m}$). These showed a continuous lumen with prescribed orientation, lined by an epithelial monolayer with tight junctions. Additionally, upregulated expression of kidney-specific functional genes compared to 2D cell monolayers indicated increased tissue functionality, as revealed by mRNA sequencing. Furthermore, our concept enabled the fabrication of hybrid tubules, which consisted of arranged subsections of different cell types, combining murine and human epithelial cells. Finally, we integrated the self-assembled fabrication into a microfluidic chip and achieved fluidic access to the lumen at the terminal sites of the tubules. With this, we realized flow conditions with a wall shear stress of $0.05 \pm 0.02\text{ dyne cm}^{-2}$ driven by hydrostatic pressure for scalable dynamic culture towards a nephron-on-chip model.

1. Introduction

Novel 3D cell culture models with enhanced physiological properties are desirable to increase predictability of organ responses *in vitro* compared to 2D cell monolayers or animal models [1, 2]. In the context of drug screening applications, the modeling of the kidney is in focus because of its role in metabolism and clearance of drugs, and its susceptibility to drug-associated cytotoxicity. In particular, the mod-

eling of the nephron tubule, which is the smallest functional unit, is considered to hold great promise for future improvements in assays for drug development, testing, and treatment optimization [3]. In sum, key structural objectives for the reconstruction of an artificial nephron tubule are (a) a hollow lumen in an extracellular matrix material, lined by (b) a closed renal epithelial cell layer, and (c) optional culture with luminal flow, to fully simulate physiological conditions. This is achieved by integ-

ration into microfluidic devices, as nephron-on-chip models [4–6]. Furthermore, for successful *in vitro* application, the models must be (d) scalable, reproducible, and parallelizable, with appropriate technological effort to fabricate large numbers of replicates.

State-of-the-art tissue engineering approaches achieved 3D tissue architectures by two main approaches, as reviewed in [4]. The first approach takes advantage of cellular self-assembly leading to the formation of epithelial cell spheroids [7–9] or tubular networks [10, 11] from randomly distributed epithelial cells within extracellular matrix materials (ECMs) without external intervention. The achieved structures provide high degrees of tissue complexity, meeting some of the mentioned tissue model requirements, and have shown increased sensitivity to nephrotoxic treatments [7, 8, 12]. The most important advantage of this approach however, stems from the fact that self-assembly increases the tissue complexity intrinsically leading to physiologically defined tissue structures. Thus, the complexity in this case does not need to be defined by technological means but is created by spontaneous self-assembly of the cells. This provides more easy handling, fabrication, and hence suitability for high-throughput applications [13]. However, the structures occur both spatially and temporarily undefined, with high variations and non-uniform size distribution of spheroids or tubules [7]. Different approaches make use of bioprinting, an additive manufacturing tool for controlling the spatial distribution of cells to fabricate 3D cellular constructs for tissue engineering. 3D-bioprinting allows for precise deposition of cell containing bioink and artificial ECMs. It was successfully used to establish various types of kidney models [14–16]. Most prominent models are based on hollow fluidic channels created in a hydrogel ECM, in which cells are seeded subsequently [14, 15, 17]. The renal epithelial cells attach to the channel walls and form an epithelial barrier after several days in culture. A fluidic connection can be established for perfused kidney-on-chip devices [15, 16]. However, this approach requires highly complex fabrication technologies, multiple manual processing steps, and specific sacrificial materials, thereby limiting the scalability of such models. Furthermore, the minimum diameter of the tubules is limited to $\sim 200\ \mu\text{m}$ [16] by the seeding process and allows for one cell type per tubule, only. The microchannel geometry decisively defines the final architecture and does not allow physiological mechanisms to adapt the geometry. All mentioned approaches either rely on immortalized cell lines, such as renal proximal tubule epithelial cells (RPTEC) [10, 15], or cells derived from induced pluripotent stem cells [18–21]. Prospectively, induced cell lines will provide great advantages, as these stem from accessible cell sources, such as fibroblasts, and therefore hold great promise for fabrication of human personalized tissue models in the future.

1.1. Bioprinting with integrated cellular self-assembly

Current bioprinting technologies provide automated solutions for handling of preformed 3D tissues as ‘building blocks’, such as spheroids [22] or larger organoids, such as tubules or strands [23]. All of these approaches aim for establishing the final tissue structure by controlled deposition and arrangement of the building blocks. In contrast to these methods, we present a novel fabrication concept, which integrates cellular self-assembly as essential element into the bioprinting fabrication approach. The capability of cells to form physiological microstructures spontaneously under certain conditions, is exploited actively to generate tissues with higher complexity and smaller micro features. Thereby no preformation and handling of 3D tissues is necessary. We generate higher tissue complexities directly in a 3D hydrogel scaffold, by self-assembly from simplified printing designs. Bioprinting combined with cellular self-assembly provides powerful mechanisms to generate complex artificial tissues for various target tissues and cell types [24, 25]. In general, post-printing cellular reorganization has to be considered when establishing new bioprinting processes, as by definition, the cellular components form an active part of the final tissue construct. Cellular reorganization adds substantial complexity to the printed tissues on both the morphological and the cellular and subcellular level, while not increasing the technological challenges of the printing process. As nicely reviewed in [26, 27], there are a variety of opportunities, such as tissue maturation and cell differentiation, but also some major challenges arise when using self-assembly in biofabrication. These are limited (spatial) control of cellular assembly on the micro-scale below the printing resolution, a reasonable reproducibility of the self-assembly and printing process and the scalability of the whole process to allow for a significant throughput. A major achievement of the present study is the successful and controlled application of the self-assembly mechanisms on a cellular level, through fabrication of well-defined active local microenvironments. We achieved those with drop-on-demand (DoD) bioprinting, which is used to fabricate simplified epithelial cell patterns with defined size and high cell density in a hydrogel ECM. With this, we investigated the fabrication of epithelial cell spheroids and nephron-like tubules systematically. All experiments were carried out with human RPTECs, a well-established reference cell line, and with a directly reprogrammed cell line derived from murine fibroblasts, induced renal tubular epithelial cells (iRECs) [7]. The cellular self-assembly concept was confirmed to work in number of different bioactive ECM materials, such as Collagen I, Matrigel, and Fibrin, and should be easily transferable to other (epithelial) cell types upon adjustment of the biomaterials to the respective cells.

2. Materials and methods

2.1. Cell culture

Immortalized renal proximal tubule epithelial cells (RPTEC/TERT1, #CRL-4031) were cultured in DMEM:F-12 medium (#30-2006) supplemented with hTERT Immortalized RPTEC growth kit (#ACS-4007, all ATCC) and G 418 bisulfate salt solution (G8168, Sigma-Aldrich) up to passage *p* 20. iRECs were cultured in DMEM (#41966029, Gibco) supplemented with 2 mM L-glutamine (#25030024, Gibco), 1% v/v penicillin/streptomycin (#P4333, Sigma), 10% v/v fetal bovine serum (#F9665, Sigma) from passage *p* 8 after isolation and expansion after direct reprogramming of fibroblasts [7]. During all conducted experiments, iRECs were cultivated in renal epithelial growth medium (#CC-3190, Lonza).

2.2. Hydrogel materials

We used different hydrogels as artificial ECM materials and for the bioink formulation. Matrigel and Collagen I, as well as Matrigel-Collagen I blends were used as ECM materials. Fibrinogen was used as a liquid carrier to suspend epithelial cells for the bioink formulation. Matrigel (Growth Factor Reduced, Phenol Red-free, LDEV-free, #356231, Corning) was used as artificial ECM material in concentrations of 100%, 66% and 33%. For printing, the Matrigel substrate was used in un-cross-linked state and cross-linking times of 30 min at 37 °C were used. Collagen I (#345236, Corning) was used as artificial ECM material in concentrations of 6, 3, and 1.5 mg ml⁻¹. From the acidic stock solution, a neutral pH was adjusted by mixing with sodium hydroxide (1 mM, NaOH), double distilled water, and PBS (10×, Sigma-Aldrich) at 4 °C. The neutralized solution was kept at 4 °C for a maximum of 1 h. Cross-linking was thermally induced by increasing the solution temperature to 37 °C for 30 min. When used as substrate material, the Collagen I hydrogel was cross-linked before printing. Matrigel/Collagen I blends were obtained by mixing the neutralized Collagen I solution (6 mg ml⁻¹) 1:1 with Matrigel 100% at 4 °C. Cross-linking for 30 min was conducted after printing. Fibrin was obtained from Fibrinogen (20 mg ml⁻¹, human plasma, #341576, Calbiochem). By mixing with Thrombin (20 U ml⁻¹, human plasma, #605190, Calbiochem) cross-linking was induced. For use as ECM material Fibrinogen and Thrombin were mixed 1:1 and cross-linked for 30 min at 37 °C. For use as bioink carrier liquid, the cell pellets were suspended in Fibrinogen, and, after deposition, cross-linking was induced by Thrombin, contained in the substrate material. To prevent enzymatic digest of Fibrin we added Aprotinin (20 µg ml⁻¹ working concentration, A1153, Sigma-Aldrich) to the cell culture medium during incubation as described in [28].

2.3. Bioink preparation

The bioink was prepared from semi-confluent cell cultures of RPTECs or iRECs. The cells were trypsinized (TrypLE, #12604013, Gibco) and centrifuged (200 g, 5 min). The supernatant was removed, and the pellet was resuspended in PBS (1 ml). The cell concentration and viability were measured by mixing the cell suspension (10 µl) with trypan blue (10 µl) and adding the stained solution to a disposable chamber slide which was inserted into an automated cell counter (Countess™ II, Thermo Fisher). The cells were centrifuged (200 g, 5 min) again, and the pellet was resuspended in Fibrinogen (FN, #341576, Calbiochem, 5 mg ml⁻¹) as carrier fluid of the final bioink. The amount of Fibrinogen volume was adjusted to achieve cell concentrations of 1×10^6 – 2.5×10^7 cells ml⁻¹. With typical droplet volumes during the bioprinting process of 10 nl, the cell concentrations were leading to droplets containing 10–250 cells, respectively.

2.4. Bioprinting

For bioprinting, we used a customized DoD bioprinter equipped with a commercial piezo driven dispenser (PipeJet®, BioFluidix GmbH, Germany). Detailed application descriptions can be found elsewhere [24, 29]. A schematic construction image of the dispenser is shown in (figure 1(a)). Disposable sterile polymer capillaries (Capillary pipes, #200-SC, BioFluidix) were mounted on the dispenser. The capillary was directly connected to pipet-tips to load the bioink. This allowed deposition of single bioink droplets with adjustable volumes between 5 and 20 nl, using a capillary nozzle diameter of 200 µm. The droplet volume can be defined in the dispenser software (BioFluidix) within the described range. Ideal piezo parameters were automatically adjusted for a stable formation of single, satellite-free droplets, with a software controlled stroboscopic camera setup (BioFluidix). The dispenser was positioned vertically above a prepared hydrogel substrate with a software controlled three-axis robotic stage, which was moving to a user defined set of XYZ coordinates. For optimized printing performance the Z-distance between dispenser nozzle and substrate surface was <5 mm. Higher distances between nozzle and substrate surface were leading to partial droplet displacements, resulting in inaccurate printing. After deposition on a hydrogel substrate, the cell containing bioink droplets formed cell patterns, which we referred to as on-site cell clusters. The single droplet clusters could be combined by overlap printing to fabricate structures in any desired design, such as lines and curves (figure 1(c)). A detailed process schematic diagram is shown in figure 1(d). First, a hydrogel layer was prepared as substrate (Layer I) on which bioink droplets were deposited, leading to on-site patterns of loosely arranged cells, as shown in the cut view schematics.

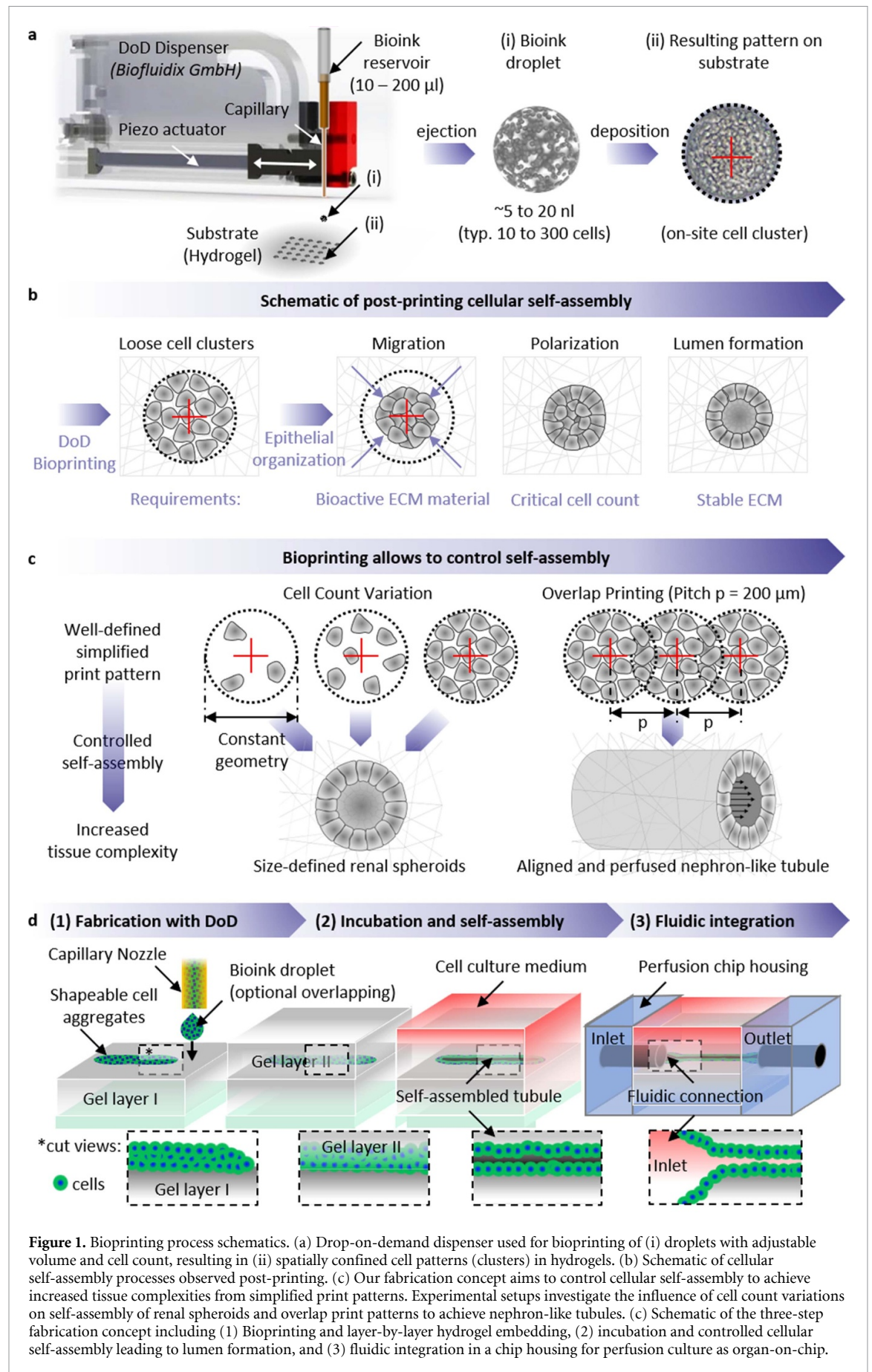


Figure 1. Bioprinting process schematics. (a) Drop-on-demand dispenser used for bioprinting of (i) droplets with adjustable volume and cell count, resulting in (ii) spatially confined cell patterns (clusters) in hydrogels. (b) Schematic of cellular self-assembly processes observed post-printing. (c) Our fabrication concept aims to control cellular self-assembly to achieve increased tissue complexities from simplified print patterns. Experimental setups investigate the influence of cell count variations on self-assembly of renal spheroids and overlap print patterns to achieve nephron-like tubules. (c) Schematic of the three-step fabrication concept including (1) Bioprinting and layer-by-layer hydrogel embedding, (2) incubation and controlled cellular self-assembly leading to lumen formation, and (3) fluidic integration in a chip housing for perfusion culture as organ-on-chip.

The printed patterns were then covered with a second hydrogel layer (layer II) for encapsulation and incubation. For both, Layer I and Layer II, pure Matrigel, Collagen I, or blends of both materials were used. Also, Fibrin is applicable for the described process. Prior to printing all materials were cross-linked for 30 min at 37 °C.

2.5. Conservation of printed cell patterns

The printed pattern of cell clusters was conserved by cross-linking of the bioink (with Fibrinogen as carrier liquid), which was catalyzed by Thrombin contained in the substrate hydrogel layer. Without Fibrinogen cross-linking, the printed pattern was scattered when the second hydrogel layer was applied, as shown in the supplemented figure S2(a) (available online at stacks.iop.org/BF/13/035019/mmedia). Bioink-FN was mandatory to conserve the cell pattern structure during this process step. This was achieved by local FN-crosslinking enzymatically induced by Thrombin (TH, 10 U ml⁻¹), which was contained in the first substrate hydrogel layer. During incubation, the loose cell clusters self-assembled and formed cellular tubules. Due to the contact-free printing process (DoD) the process could be conducted on-chip (figure 1(d)), with open bottom chip designs. After housing and sealing, the cells self-assembled to tubules, and the lumen was connected for fluidic perfusion with self-assembled funnel structures at the in- and outlet connector ports.

2.6. mRNA extraction and sequencing

Messenger RNA (mRNA) was extracted from printed iRECs and iRECs seeded in 2D after 7 d of incubation. Each experiment was performed three times at intervals of 2.5 weeks, corresponding to passages p35, p43 and p52. For each condition, eight identical samples were seeded at day 0 with 6000 cells each. mRNA was extracted using the Trizol based RNeasy Plus Universal Mini Kit (Qiagen, #73404) with slight modifications as suggested by Khetan and Burdick for 3D hydrogels [30]. mRNA samples were sequenced on an Illumina HiSeq platform and 150 bp paired-end reads were generated (Novogene, HK).

2.7. Transcriptomic analysis

Sequenced datasets were uploaded to the Galaxy platform [31]. After a quality check with FastQC (version 0.72), paired reads were trimmed with Trim Galore! (version 0.4.3) and aligned to the reference mouse genome mm10 with RNA STAR (version 2.6.0b-1) [32]. Reads were counted with featureCounts (version 1.6.3) [33] and differential expression analysis was run with DESeq2 (version 1.22.1) [34] considering each microenvironment and individual replicate as a factor. As all samples passed the quality control, further bioinformatic analysis was conducted on Rstudio (version 1.1.456). When referring to kidney specificity, gene expression in mouse kidney

with respect to the median of the other mouse tissues were compared, according to the RNA sequencing based expression analysis from [35]. The gene ontology (GO) enrichment analysis was run with clusterProfiler (version 3.10.1) with a *p*-value cutoff of 0.01, corrected with the Benjamini–Hochberg method, and a *q*-value cutoff of 0.05 [36]. Volcano plots and heatmaps were made with R packages ggplot2 (version 3.2.1) and heatmap.plus (version 1.3).

2.8. Fluidic chip integration

The perfusion chip setup consisted of a milled PMMA base, with six parallel open channel cavities in which the substrate hydrogel was prepared for on-site cell clustering by bioprinting. Immediately after printing the base was housed with a commercial open bottom perfusion chip (sticky-Slide VI 0.4, ibidi GmbH, Germany) and sealed with an adhesive interlayer. Then the printed cell patterns were covered with a second hydrogel layer by pipetting and incubated in cell culture medium. Photographs of all parts are shown in supplemented figure S3(c).

2.9. Imaging

Brightfield (BF) and fluorescence of green fluorescent protein (GFP) microscope images were acquired with an inverted microscope (Axio Observer 7, Carl Zeiss) with a 10×/0.30 objective (EC Plan Neofluar, Zeiss). BF images were acquired with TL Halogen Lamp illumination. For fluorophore (GFP) excitation, LED transmission illumination was used with filter wavelengths of 473–496 nm (excitation) and 511–528 nm (emission). Confocal microscopy was performed using a laser scanning microscope (LSM-I-NLO, Carl Zeiss) equipped with a 40×/0.80 W objective (Achromplan, Zeiss). Fluorophore excitation was performed with a single-photon laser at 488 nm (GFP) and 561 nm (Cy 3). For image analysis, ZEN Blue (Version 2.6, Zeiss) and ImageJ software were used. A major challenge of confocal imaging was high background noise, caused by the biopolymer hydrogels, and low signal intensities, due to the increased thickness and absorption of 3D constructs, compared to 2D cell monolayers. Also the antibody staining protocol had to be adapted to these conditions, as described in [24].

2.10. Data acquisition and statistics

Presented microscope images are representative from at least three independent experimental runs. Spheroid size measurements were conducted for 49 structures per experiment, with three individual experimental runs. A schematic of the experimental setup is shown in supplemented figure S3(a). The spheroid size was determined from fluorescence microscope images (threshold below 96.5%, 8 bit gray values). From this, mean values and standard deviations (SD) were calculated for each experimental run. The error of the mean was calculated from the individual

SD values. The width of nephron-like tubules was determined for at least five samples, at three positions along the tubules. Mean Day 0 cell cluster extensions and volume were determined from four independent confocal Z-scans in three independent experimental runs (ZEISS ZEN blue 3.1). The spheroid formation rate was determined from fluorescence images; spheroids were considered as successfully formed when geometrical (roundness >70%) and morphological criteria were met, e.g. one single, continuous cell aggregate with membrane-like boundary to the ECM was formed. In contrast, spheroid formation was considered to be not successful when cells remained singularized, spread or aggregated in multiple smaller fractions. Datasets were tested for normal distribution using Saphiro–Wilk, rejecting the null hypothesis for p -values < 0.05 (OriginPro 2019). To analyze variances between non-normal distributed datasets, these were compared with Kruskal–Wallis ANOVA (OriginPro 2019), with a significance probability threshold of $\chi^2 < 0.05$.

3. Results and discussion

To establish a process that provides reproducible, spatial, and temporal control over epithelial cell self-assembly of three-dimensional (3D) spheroids and nephron-like tubule structures, we investigated a compatible set of a scaffold material for an artificial ECM, a technology for bioprinting that enables the precise and automated deposition of cells, and a suitable cell containing bioink for printing. To provide proof of transferability of all presented results, these refer to corresponding experiments conducted with murine directly reprogrammed iREC and human primary RPTEC cell lines.

3.1. Matrigel, Collagen I and Fibrin promote epithelial cell self-assembly

We selected suitable materials for the artificial ECM with respect to cell related physicochemical properties and bioprinting process compatibility. This implied mechanical stability, degradation and hydrogel bioactivity, which promotes the appearance of desired morphologies of embedded epithelial cells, such as self-assembly of spheroids and tubules. Second, the materials were tested for compatibility with the intended layer-by-layer bioprinting process, which includes cross-linking mechanisms, bulk and surface homogeneity, and low batch-to-batch variations. We tested common hydrogel materials, in different concentrations, which showed good cyto-compatibility in previous studies: Matrigel (100%, 66%, 33%) [7], Collagen I (3, 1.5 mg ml⁻¹) [37], Fibrin (10 mg ml⁻¹) [38, 39], and Collagen/Matrigel blends (1.5 mg ml⁻¹, 50%), respectively. To test the cell related properties, epithelial cells were suspended in the un-cross-linked materials to achieve a random and isotropic cell distribution in the scaffold with a final concentration

of 1×10^5 cells ml⁻¹. After cross-linking, we incubated the constructs for 7 d for microscopic observation of cell morphologies (supplemented figure S1). Previous studies have shown that within such constructs, depending on cell density and spatial cell distribution, the hydrogel embedded epithelial cells randomly self-assemble to complex spheroids, or tubular networks, with nephron-like cell polarization and localized expression of membrane transport proteins [7, 10]. Here, we were able to reproduce these processes in three tested materials at different concentration conditions. Epithelial cells showed changing morphologies compared to Day 0, with self-assembly of spheroid-like structures in Matrigel, Collagen and Fibrin with all tested concentrations. The spheroids were randomly distributed in the hydrogel and showed high size variances. These results coincided with previous studies in pure Matrigel [7]. In contrast, inert materials, such as Agarose and Alginate, showed unchanged single cells, with round cell morphologies during the entire incubation period (data not shown). Fibrin showed fast and complete enzymatic degradation in the presence of embedded epithelial cells, which could be evaded by addition of Aprotinin (20 μ g ml⁻¹), however bearing potentially unknown adverse treatment effects. In terms of physical properties a comprehensive and systematic overview of rheological parameters of the hydrogels including a head-to-head comparison of dynamic mechanical storage and loss moduli was previously conducted and presented in [40, 41]. In general, the mechanical stability is increasing with the biopolymer concentration. Of the suitable materials, Matrigel provides the highest storage modulus (100%, 85 Pa), followed by Collagen I (3 mg ml⁻¹, 33 Pa) and Fibrin (10 mg ml⁻¹, 16 Pa). For all materials, the tested concentrations mainly affected the mechanical stability of the constructs, while the epithelial cell morphology could be considered independent from that parameter. The dynamic elastic moduli of the used ECM materials are considerably low compared to the stiffness of physiological tissues, which should be considered in the range of 1–10 kPa [42, 43]. Although these values are not fully comparable as they are determined by very different measuring methods, a deviation was to be expected, since a high proportion of ECM volume is still acellular in our models. The approximation of matrix stiffness to physiological conditions and the research on its impact on cell behavior are important points for future studies, but beyond the scope of this work. For subsequent experiments, we therefore used the highest possible concentration to maximize construct stability and integrity, and to enable fluidic integration into chip housings for perfusion. With respect to the bioprinting process compatibility, temperature induced cross-linking mechanisms of Matrigel and Collagen I provide a flat and chemically homogeneous hydrogel surface composition. We identified this

Table 1. Overview of drop-on-demand process parameters. Five bioinks with varying concentrations (c_x) or induced renal epithelial cells (iREC) were printed, to achieve droplets with defined target cell counts (*ideal droplet volume of 10 nl). Mean measurement values with standard deviations (SD) of three individual experiments are shown. The actual cell count per droplet was calculated from the measured cell concentration of 100 droplets (diluted in 10 μ l). The respective cell count accuracy was calculated relative to the target values. Post-printing cell-viability was determined by Trypan-blue staining.

	Target cell count (cells drop ⁻¹)	Required bioink concentration* (cells ml ⁻¹)	Measured cell concentration \pm SD (100 drops in 10 μ l) (cells ml ⁻¹)	Calculated actual cell count* (cells drop ⁻¹)	Mean cell count accuracy	Mean cell viability
c ₁	10	1×10^6	$9.2 \times 10^4 \pm 2.4 \times 10^4$	9.2 ± 2.4	$79 \pm 26\%$	92%
c ₂	50	5×10^6	$5.0 \times 10^5 \pm 8.8 \times 10^4$	49.8 ± 8.8	$87 \pm 18\%$	92%
c ₃	100	1×10^7	$1.2 \times 10^6 \pm 5.5 \times 10^4$	115.3 ± 5.5	$85 \pm 5\%$	91%
c ₄	150	1.5×10^7	$1.9 \times 10^6 \pm 4.8 \times 10^4$	185.1 ± 4.8	$77 \pm 3\%$	91%
c ₅	250	2.5×10^7	$2.9 \times 10^6 \pm 6.8 \times 10^4$	293.4 ± 6.9	$83 \pm 2\%$	93%
Overall Mean \pm Error of the Mean					$82 \pm 6\%$	$92 \pm 2\%$

as key property to establish a stable and reproducible layer-by-layer bioprinting process. Especially the wetting behavior of the bioink printed onto hydrogel surfaces was homogeneous and reproducible for these materials. In contrast, the two-component-induced cross-linker Fibrin showed uneven surface geometries or chemically inhomogeneous surface properties, leading to unpredictable bioink wetting and limited reproducibility of print patterns.

3.2. DoD bioprinting enables precise and gentle handling of cell suspension bioinks

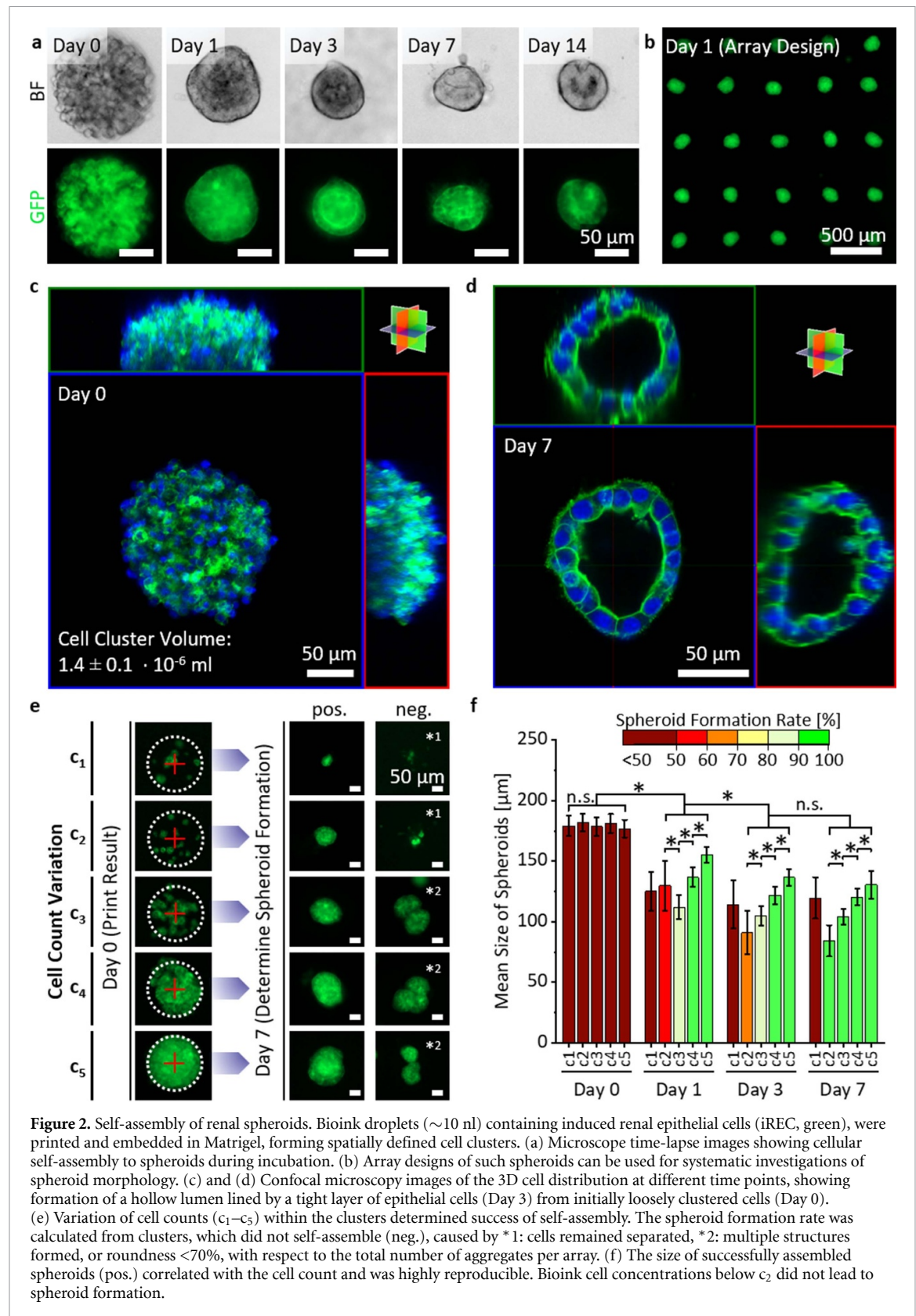
For controlled deposition and embedding of cells within the artificial ECM material, we formulated a cell suspension bioink with fibrinogen as liquid carrier and applied DoD bioprinting technology. To determine cyto-compatibility and the precision of the process, we first characterized key technological and cell-related parameters, as summarized in table 1. The first important technological parameter was considered as the droplet volume, for which we determined a coefficient of variation (CV). The droplet volume was set to a target volume of 10 nl by adjusting the piezo parameters of the DoD dispenser. We optically determined the droplet volume of single droplets containing 2.5×10^7 cells ml⁻¹ in a stroboscopic setup, revealing a mean volume of $V_{\text{droplet}} = 10.96 \pm 1.01$ nl, with a respective CV = 9.25% ($n = 7000$). This variation could be related to the presence of high amounts of cells and biopolymers in the bioink, which cause inhomogeneity of the bioink properties, which directly affects the droplet formation at the nozzle. To evaluate cell-related printing parameters, we measured the cell viability and cell count accuracy. We printed 100 droplets (1 μ l total volume), with five different cell concentrations, in three independent experiments, respectively. The accumulated volume of 100 droplets was diluted (1:10) to 10 μ l total volume and mixed with Trypan Blue for counting of dead and viable cells, which was measured using an automated cell counter. The measurements showed a high post-printing cell viability of $92 \pm 3\%$, without influence

of the cell concentration in the bioink. The high viability could be related to the comparably low viscosities of the processed bioink of 1.6–38.5 mPa s (shear rate dependent), thus, low shear stresses occur during the printing process. The cell count measurements revealed a calculated overall mean cell count accuracy of $82 \pm 6\%$ with respect to the desired cell number per droplet. The absolute cell count variation was in the same order of magnitude for all cell concentrations. However, the relative variation from the target value was highest for low absolute cell counts per droplet, where CVs of $\pm 26\%$ (10 cells) and $\pm 18\%$ (50 cells) were calculated. The three higher concentrations varied $\pm 5\%$ or lower.

Major error sources of the droplet accuracy are related to the preparation and adjustment of the bioink cell concentration, which is again based on previous cell count measurements and dilution steps. Additionally, the droplet volume CV, and cell sedimentation in the bioink can influence the cell count accuracy but were not investigated separately. In sum, the characterized DoD bioprinting technology allows to deposit well-defined bioink droplets with adjustable cell counts per droplet and high cell viability.

3.3. DoD bioprinting allows on-site cell aggregation for spatially controlled self-assembly

After characterizing the process parameters of the used DoD bioprinting technology, we tested its capability to spatially control epithelial cell self-assembly and to achieve reproducible spheroid formation at defined positions within an artificial ECM. Therefore, we printed bioink droplets containing iRECs on a first hydrogel layer for on-site cell clustering with defined cell density and embedded them with a second hydrogel layer for incubation and microscopic observation. Each droplet thereby formed one separated cell cluster. A representative microscope image of a cell cluster is shown in figure 2(a) (Day 0). Both cell types, iRECs and RPTECs, and Matrigel and Matrigel/Collagen blends as ECM materials were used to confirm the presented results. For systematic measurements,



we implemented an array design with a defined drop-to-drop distance (pitch) of $p_{\text{Array}} = 500 \mu\text{m}$, as shown in figure 2(b).

Immediately after fabrication (Day 0) the clusters consist of spatially confined, loosely arranged cells in a spheroidal shape. In Matrigel 100%, a mean

lateral extension of $W_{\text{Matrigel}} = 180 \pm 10 \mu\text{m}$, and a mean vertical extension of $h = 79 \pm 2 \mu\text{m}$, with a corresponding volume of $V_{\text{Cluster}} = 1.4 \pm 0.1 \times 10^6 \mu\text{m}^3$ were determined from confocal microscopy scans, as shown in figure 2(c) ($n = 4$). The volume was significantly reduced to $14 \pm 1\%$ compared to

the initial droplet volume, which is mainly related to a vertical compression and lateral extension (surface wetting) of the droplet volume during the impact on the surface. Depending on the used substrate material this effect is altered, as for Collagen I the lateral width is increased to $W_{\text{Collagen}} = 285 \pm 81 \mu\text{m}$. Microscopic time-lapse images showed post-printing cellular reorganization, which can be summarized as a cellular densification process. A schematic description of the underlying processes is shown in figure 1(b). This resulted in cell aggregation with decreasing overall volume, mainly caused by decreasing lateral size, and in the formation of inter-cellular contacts. This included the formation of a sharp, membrane-like boundary to the ECM within the first day of incubation, the formation of cell-cell contacts and a resulting closed epithelial cell layer. The aggregate sizes continuously decreased within the first 7 d of incubation. The subsequent incubation period until Day 14 did not lead to a significant decrease in aggregate size. To confirm successful self-assembly of spheroids, we characterized the final cell arrangement at Day 7 of incubation by confocal microscopy scans, showing the formation of a spheroid structure, comprising a lumen, lined by a continuous epithelial cell layer (figure 2(d)). These observations coincide well with described renal spheroid formation in literature [20]. The cell count per spheroid was determined by counting positively stained nuclei. The cell count at Day 7 correlated well with the initially printed cell count at Day 0 ($n = 3$). These results are in line with state-of-the-art reports, showing self-assembled spheroids in Matrigel, with high degrees of renal marker gene expression [7]. Here, we advanced the self-assembly process by gaining control over spatial appearance within a hydrogel scaffold. Furthermore, the on-site aggregation and self-assembly directly led to hydrogel embedded spheroids, which provided a 3D environment. This provides additional benefits over hanging drop or suspension culture formation [9], as no further complex spheroid handling is required for 3D ECM embedding.

3.4. Control of local cell density allows reproducible fabrication of size-defined spheroids

To test the hypothesis that we can spatially control and guide the cellular self-assembly process, we fabricated clusters with varying cell numbers, as schematically shown in figure 1(c), embedded them in a Matrigel ECM and investigated the resulting epithelial cell spheroid formation. This was achieved by bioprinting of droplets with five different bioink cell concentrations as summarized in table 1, resulting in a single confined clusters with well-defined cell counts. During culturing of these arrays, we measured the individual spheroid sizes, in correlation to the initial cell count per cluster. Furthermore, we determined the spheroid formation rate as the number of positively formed spheroids (pos.) over the total number of

printed clusters, shown in figure 2(e). Mean values from 49 individual spheroids, from three independent experiments, with an observation period of 7 d, are shown in figure 2(f). The initially bioprinted clusters showed a mean size of $179 \pm 4 \mu\text{m}$ at Day 0, with no significant difference between all tested cell concentration conditions ($p = 0.34$). All clusters aggregated and decreased in size during the first day of incubation, indicating a cellular densification process. However, depending on the used cell concentration, some aggregates did not successfully form spheroids. At Day 1 the three highest cell concentrations showed a spheroid formation rate of $>90\%$. The mean size correlated to the absolute cell number and was determined to $155 \pm 7 \mu\text{m}$ (250 cells per aggregate), $137 \pm 8 \mu\text{m}$ (150 cells), and $112 \pm 10 \mu\text{m}$ (100 cells), respectively. The two lower concentrations showed a spheroid formation rate of $<60\%$ without size to cell number correlation, caused by aggregates with reduced densification, and mean sizes of $130 \pm 21 \mu\text{m}$ (50 cells) and $125 \pm 16 \mu\text{m}$ (10 cells). At Day 3, the size further decreased for all conditions. At this time point, the four highest cell count conditions showed significantly differing sizes, in correlation with different cell numbers with $137 \pm 7 \mu\text{m}$ (250 cells), $122 \pm 7 \mu\text{m}$ (150 cells), $105 \pm 6 \mu\text{m}$ (100 cells), and $84 \pm 13 \mu\text{m}$ (50 cells). Between Day 7 and Day 14 no significant change in spheroid size was detected for all conditions ($p > 0.05$), leading to final spheroid sizes of $131 \pm 11 \mu\text{m}$ (100%, 250 cells), $120 \pm 7 \mu\text{m}$ (100%, 150 cells), $104 \pm 6 \mu\text{m}$ (100%, 100 cells), $84 \pm 13 \mu\text{m}$ (75%, 50 cells) with significant cell number to spheroid size correlations. These sizes are in good accordance with the expected size to cell number correlation from a theoretical spheroid model, which is illustrated in supplemented figure S3(b). Moreover, the observed spheroid dimensions cover the reported size range in literature [7, 9, 20]. For the lowest cell count we found a final size of $120 \pm 17 \mu\text{m}$ (45%, 10 cells). We assume that the used cell concentration resulted in aggregates below a critical minimum cell density, leading to ineffective spheroid formation. The increased size compared to higher cell concentrations was related to deficient densification and migration, causing unguided cell growth of individual cells. Overall, the results confirmed, that DoD bioprinting enabled the fabrication of size defined spheroids with defined cell numbers. From these aggregates, self-assembly lead to the formation of spheroids with pre-defined final sizes. Furthermore, from the five tested cell concentrations, we defined a critical initial cell number of $N_{\text{cells}(c_2)} = 50 \pm 9$ cells in a volume of $V_{\text{Agg.}}$, resulting in a critical local cell concentration of $c_{\text{critical}} = 3.7 \pm 0.2 \times 10^7 \text{ cells ml}^{-1}$ necessary for cells within one aggregate to interact and self-assemble to a single spheroid. However, to absolutely define the critical cell concentration value, a bioprinting technology with higher spatial resolution and cell count accuracy would be beneficial,

ideally providing single-cell resolution. Additionally, the cell count might be altered during incubation by necrosis, apoptosis or cell proliferation. However, as the key success or failure for self-assembly was already determined within the first 24 h of incubation, and the cell count between Day 0 and Day 7 did not significantly differ, we assume that these effects can be neglected.

3.5. Line shaped patterns self-assemble to nephron-like tubules

To realize customizable and scalable tissue designs beyond spheroids, we combined single droplets by overlap printing (figure 1(c)). For this, we defined an ideal substrate material and corresponding overlap pitch. First attempts failed, based on Matrigel 100% substrates, as the overlap printing resulted in discontinuous patterns. This was potentially caused by local penetration and encapsulation of the individual deposited droplets into the semi-liquid, Matrigel surface. Furthermore, Matrigel 100% surfaces were partly non-adhesive for deposited droplets and therefore unsuitable for successful patterning by bioprinting (supplemented figure S2(b)). Alternatively, we tested Collagen I (3 mg ml⁻¹) and Matrigel/Collagen I (3 mg ml⁻¹/50%) blends to improve the surface properties of the substrate material. For both material compositions, we achieved the desired continuous fusion of building blocks when printed with an overlap pitch of 200 μ m. In a first step, we fabricated line-shaped cell patterns with a length of 15 mm by overlapping 75 droplets. This resulted in spatially confined cell clusters with a cylindrical shape. Within the clusters we found a homogeneous cell distribution (figure 3(a)), similar to the previously described spherical distribution (figure 2(c)). During the first days of incubation, the clusters aggregated and showed identical cellular reorganization mechanisms as described for the spheroids, including cell migration, densification, formation of a membrane-like boundary, and cell-to-cell contacts, as shown in the time-lapse microscope images. As a result, a tube-shaped cell aggregate was formed. We hypothesize that the underlying self-assembly mechanisms are characteristic of many epithelial cell lines, as observed in previous studies [7, 37]. Furthermore, these cells tend to form tubules in decellularized kidneys showing the capacity to self-organize to a high-dimensional cell assembly, as also observed in tissue morphogenesis from renal progenitor clusters [44]. A remaining challenge, which was not in the scope of this work, was the identification of specific cellular mechanisms that were involved in this process. Based on our fabrication concept, as well-controlled platform technology, future investigations could include long-term live confocal cell imaging, active gene regulation, cell migration and apoptosis. In this work, we identified a correlation of initial cell density on the successful self-assembly of a

continuous tubule with predefined geometry. Bioink concentrations below 100 cells ml⁻¹ (c_3) resulted in discontinuous, partly undefined tubule geometries after self-assembly (supplemented figure S2(c)). Continuous tubules were achieved with bioink cell concentrations c_3 , c_4 and c_5 . However, the resulting tubule diameter was not significantly influenced by that parameter. With successfully self-assembled nephron-like tubules, we performed confocal laser scan microscopy to reveal the 3D cell arrangement. This showed that cellular self-assembly led to a compact tubular construct at Day 1, with a closed cell arrangement in a tubular form, but without a central lumen. Again, as observed for spheroid assembly, cellular migration led to an aggregation and densification of the cell distribution compared to Day 0, where the line width was determined to $w_{\text{Day } 0} = 267 \pm 4 \mu\text{m}$ (figure 3(b)). Self-assembly included the formation of cell-to-cell contacts, shown in figure 3(c), causing a decreased lateral size distribution on Day 1 ($w_{\text{Day } 1} = 153 \pm 76 \mu\text{m}$). The size variation along the tubules was relatively high, indicating that the self-assembly process was still ongoing. Subsequent incubation days led to a more uniform size, and a change in the construct organization. We observed the formation of a lumen, present from Day 4 (figure 3(c)) and a final width $w_{\text{Day } 4} = 98 \pm 13 \mu\text{m}$. We hypothesize, that cell polarization induced a disintegration of apical cell-to-cell contacts, thereby formation of a cellular monolayer lining the lumen. A single layer of epithelial cells lined the hollow lumen, which was in good accordance to described self-assembly of nephron-like tubules in literature, with coinciding sizes [10]. The formed epithelium showed continuous tight junctional connections, as demonstrated by positive ZO1 staining (figure 3(d)), also coinciding with reported self-assembled 3D cell polarization and functionalization [7]. Further incubation up to Day 28 did show significant changes in tubule width. We conclude that the shrinking of the tubular diameter is a consequence of cellular re-organization mechanisms after the printing process, when the tubule adopts its final and highly ordered morphological structure.

3.6. DoD enables fabrication of custom cellular designs and hybrid cell models

To demonstrate the range of possible designs, which can be realized with the presented DoD bioprinting process, we fabricated tissue designs beyond spheroid arrays and line-shaped tubular constructs. For this we defined an arbitrary and scalable perimeter, representing the desired design, and subdivided it by a set of coordinates with a constant pitch of 200 μ m, to realize a continuous and homogeneous drop-to-drop overlap. With this, we fabricated convoluted tubular constructs consisting of 545 combined single droplets and a corresponding total length of 100 mm. The fabricated cell pattern again successfully

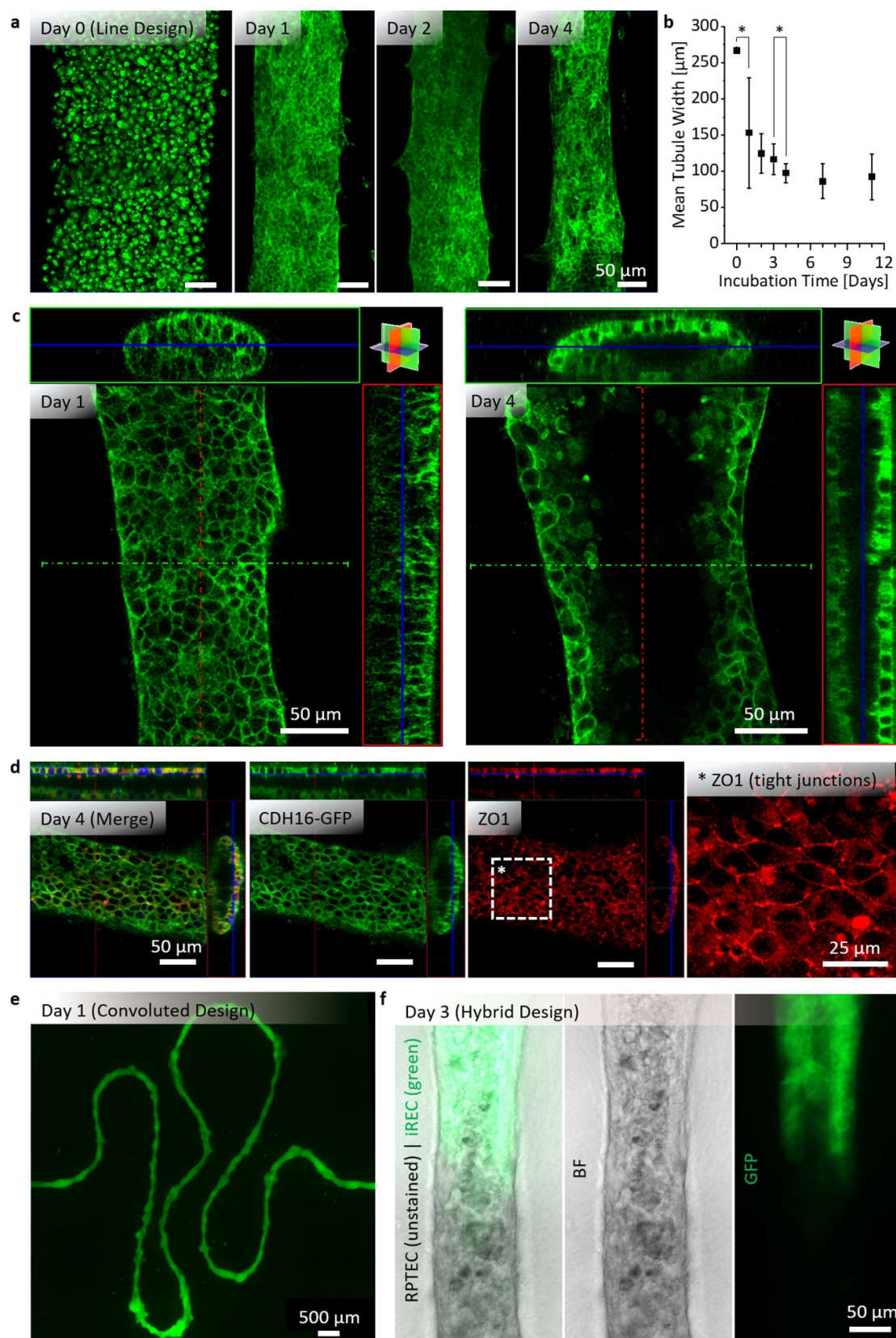


Figure 3. Self-assembly of renal nephron-like tubules. (a) Fluorescence microscope images of a bioprinted line pattern of induced renal epithelial cells (iREC) with CDH16-GFP (green), embedded in a Collagen|Matrigel (3 mg ml^{-1} | 50%) hydrogel (Day 0) and subsequent self-assembly of nephron-like tubules. (b) Mean width of tubules during self-assembly until Day 11 of incubation. (c) Confocal scan images show cell organization and lumen formation between Day 1 and Day 4. (d) Immunostaining shows positive formation of tight-junctions. (e) Self-assembled convoluted tubule design fabricated with drop-on-demand bioprinting. (f) Hybrid tubule comprising of combined sections of human RPTEC (unstained) and murine iREC (green).

self-assembled and formed a convoluted tubule structure (figure 3(e)). With this, we could show that our DoD bioprinting approach allows fabrication of similar designs as previously shown with extrusion based bioprinting approaches [15]. However, besides the method used for patterning, the here described self-assembly mechanism would also be applicable for extrusion-based dispensing technologies, which was not in the scope of this work. To highlight an exclusive advantage of DoD bioprinting over extrusion-based and cell seeding based approaches, we fabricated tubular patterns comprising more than one cell type. A discontinuous cellular arrangement was achieved by combining droplets containing different cell types (iREC and RPTEC), in one hybrid tubular construct. Therefore, the printer setup was equipped with a second dispenser channel. The two dispenser reservoirs were filled with the respective bioink (Bioink 1: iREC, Bioink 2: RPTEC, both $c = 1 \times 10^7$ cells ml^{-1}) and assigned to an individual set of coordinates, respectively. With this, a line shaped aggregate with 15 mm total length was fabricated, consisting of two subsections of iRECs and RPTECs, with a cell transition located in the center (figure 3(f)). The entire aggregate self-assembled and formed a tubular construct, as described before. The two cell types merged at the transition and formed a continuous hybrid cell layer. This shows that murine and human renal epithelial cell types can be combined in hybrid cell models. Prospectively, such an approach could be used to fabricate renal tubule constructs and to reproduce the subsections of a whole nephron, including e.g. proximal tubule, loop of Henle, distal tubule, and collecting duct. The technological challenge of this approach is the complex spatial alignment of different DoD dispensers, which deposit the respective cell types at prescribed coordinates, in order to achieve continuous overlap and transition regions of different cell types. Furthermore, different types of cells require optimized culture media compositions, which must be developed for hybrid cell models.

3.7. Bioprinted self-assembled tubules show upregulated kidney-specific functional genes

To determine how cellular processes are affected on a molecular level in the bioprinted self-assembled tubules, we subjected self-assembled tubules of iRECs and conventionally plated iRECs in 2D monolayers to RNA-Seq analysis. The transcriptome of self-assembled tubule samples showed a total of 481 significantly ($\text{Padj} < 0.05$) differentially expressed genes (figure 4(a)). We found that 379 genes (78.8%) were upregulated, while only 102 genes (21.2%) were downregulated in bioprinted and self-assembled iREC tubules. GO-term analysis revealed enrichment in cellular processes, such as response to fibroblast growth factor and organic anion transport, both of which are relevant to the formation of tubular kidney structures *in vivo* (figure 4(b)) [45–47]. Among

the robustly up-regulated transcripts ($\log_2\text{FC} > 1$), we found 34 to be enriched in the kidneys with a median expression level two times higher than in other tissues (figure 4(c)). Among these kidney specific genes are transcripts that encode for the sodium bicarbonate cotransporter *Slc4a4*, the glucose responsive transcription factor *Mxipl*, and *Ramp3*, involved in renal calcium excretion. In addition, we detected an increased expression of kidney specific transmembrane proteins, transporters and regulators, such as *Slc6a12*, *Slc5a6*, *Srcin1*, *Ksr2*, *Tmem229a*, *Tspan8*, *Sgms2* and *Fetub*. Consistent with the observation that tubules in the printed samples formed tight epithelial junctions, we observed strong upregulation of *Scel*, present in epithelia with barrier properties, and *Cldn4*, a claudin family member at tight junctions. Interestingly, printing and guided tubule formation promotes up-regulation of *Ugdh*, a gene participating in the biosynthesis of glycosaminoglycans, common components of the extracellular matrix. These results show that bioprinted directly reprogrammed renal cells not only retained their state of differentiation, but that the kidney specific gene signatures were enhanced.

3.8. Self-assembled tubular structures can be integrated in a chip for perfusion culture

Finally, we investigated options to access the lumen of the self-assembled tubules and established fluid flow conditions, which, to our knowledge, has not yet been described in literature. Yet, luminal flow is one of the key requirements to approach physiological conditions in culture. To achieve this, we identified another self-assembly mechanism occurring simultaneously with the above described self-assembly of tubular geometries. With an appropriate construct design, this second mechanism resulted in terminal openings of the lumen at both ends of the tubules. By predefining the orientation of the lumen, bioprinting then allowed to connect input and output ports of a chip housing. Schematic images of the conducted process steps are shown in figure 5(a). We used bioprinting for on-chip clustering of epithelial cells on a Collagen I substrate (COL layer I). The patterns were designed as straight lines with 15 mm length, which connected the inlet and outlet ports of the final chip setup. Next, the substrates were housed with an open cavity channel slide as counterpart (*Sticky Slide VI*, *Ibidi*, Germany). We then applied un-cross-linked Collagen I (COL layer II) to partly encapsulate the cell patterns with artificial ECM material. A photograph of the completed setup is shown in the supplemented figure S3(c). The terminal parts of the cell patterns remained uncovered, i.e. they were not encapsulated by the second Collagen I layer, as schematically shown in figure 5(d). This was mandatory to enable subsequent self-assembly of terminal lumen access. After cross-linking, we applied cell culture medium and incubated the housed constructs. With

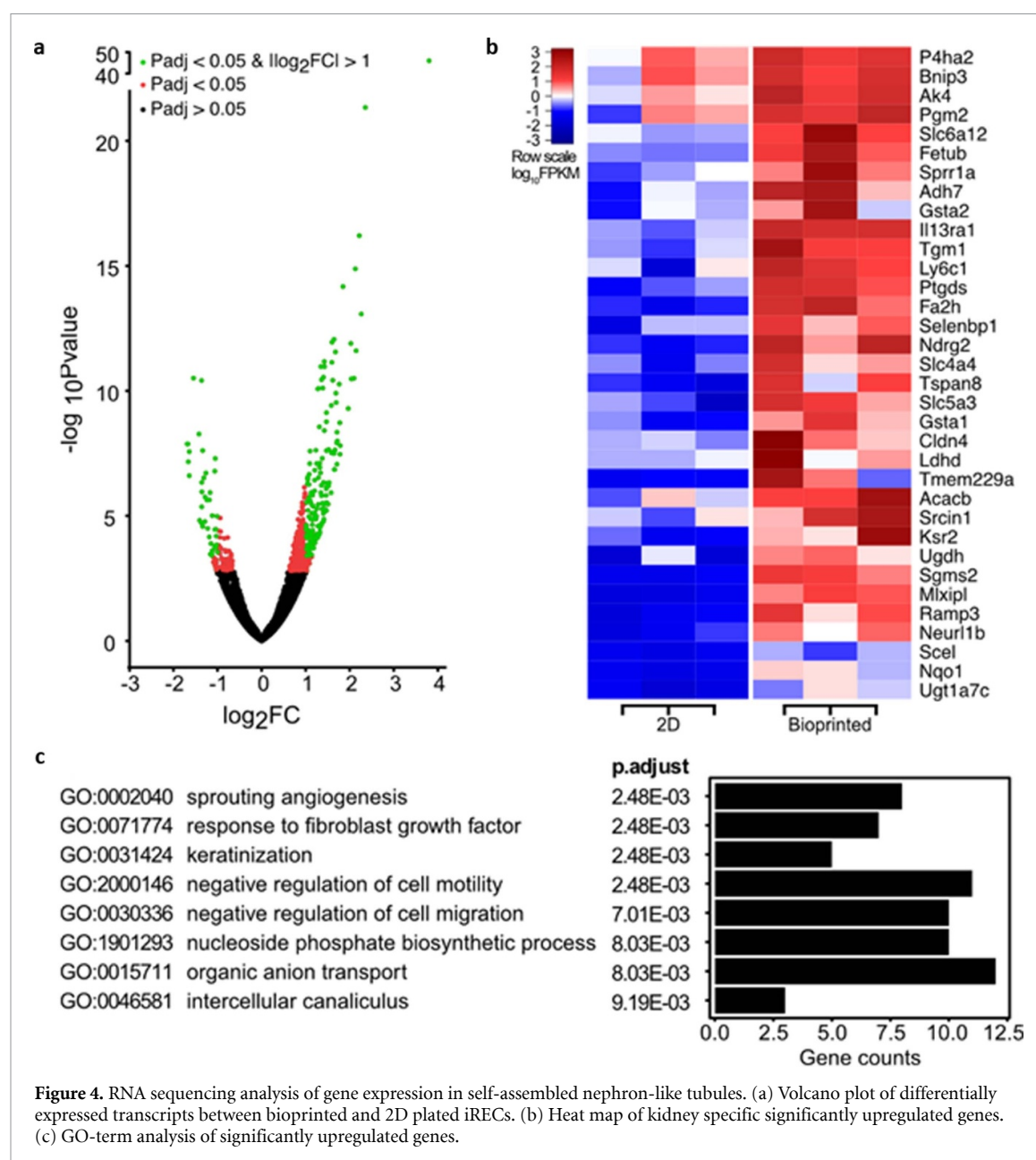
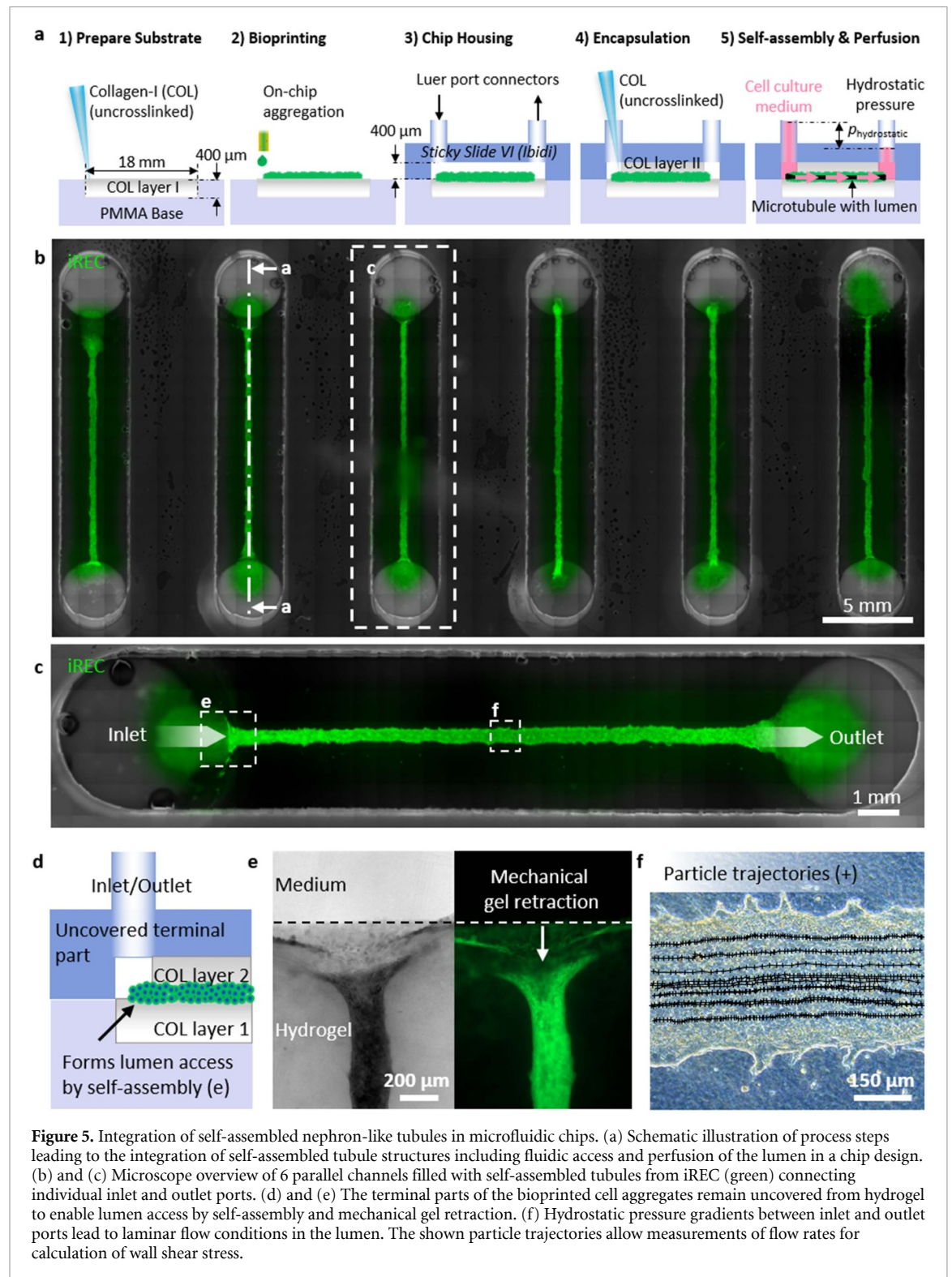


Figure 4. RNA sequencing analysis of gene expression in self-assembled nephron-like tubules. (a) Volcano plot of differentially expressed transcripts between bioprinted and 2D plated iRECs. (b) Heat map of kidney specific significantly upregulated genes. (c) GO-term analysis of significantly upregulated genes.

this, a cell to medium interface was generated. During the first days of incubation we observed the described self-assembly process leading to the formation of nephron-like tubules. Along the tubules, some cells formed protruding structures into the hydrogel (figure 5(f)). These structures were present from Day 1 of incubation and did not significantly change their shape during further incubation times. They might be caused by cellular migration processes. We hypothesize that this phenomenon was due to mechanical and chemical cell–matrix interactions between tubular cells and the adjacent hydrogel. In consequence of secreted proteases, the ECM might be locally degraded, which allowed single cells to evade the tight tubular organization.

Furthermore, matrix induced mechanical forces might interact with the tight epithelial layer. Although lateral protrusions were observed, the

tubules were stable during the time course of the experiments and the phenomenon did not lead to disintegration of printed structures or disruption of lumen formation. As laminar flow was not affected, we do not assume that the luminal epithelial cell layer based on strong cell–cell interactions and tight junctions was impaired by these basolateral migration processes. Additionally, the terminal freestanding parts of the aggregates self-assembled to funnel like openings of the lumen (figure 5(e)). The funnel shape was generated by cells, which were mechanically retracting the ECM material in direction of the tubules, caused by the cellular densification process. With this effect, we achieved fluidic connection of up to six separately accessible, self-assembled tubular structures (figure 5(b)) after four days of incubation. Fluid flow in the lumen was driven by hydrostatic pressure ($p_{\text{hydrostatic}} \approx 2 \text{ mbar}$), which we generated



in the chip connector ports, serving as reservoirs. By addition of polystyrene particles ($\varnothing = 10 \mu\text{m}$) to the perfusate, we imaged the particle flow within the lumen (Supplement Video V1), to determine the fluid flow conditions within the tubules. Therefore, we measured the particle movement by determining the respective positions in the image sequence ($n = 25$). This revealed laminar flow conditions within the completely unclogged lumen, as shown by straight

particle trajectories (figure 5(f)). The mean particle velocity, representing the 3D flow profile within the lumen, was determined to $v_{\text{mean}} = 396 \pm 149 \mu\text{m s}^{-1}$. From this we calculated a volumetric flow rate of $Q = 4.9 \pm 1.8 \times 10^{-3} \mu\text{l s}^{-1}$. The tubule geometry was calculated from the measured height ($63 \mu\text{m}$) and the width ($250 \mu\text{m}$) from microscopic images. Based on the geometry and the determined flow rate Q we calculated the maximum wall shear stress of

$\tau_{\max} = 0.05 \pm 0.02 \text{ dyne cm}^{-2}$ ($5 \pm 2 \times 10^{-3} \text{ Pa}$). These values are in good accordance to reported physiological flow conditions in rats, as described in [48], and previously used conditions in nephron-on-chip devices [15, 16]. We generated the hydrostatic pressure by tilting the chip around the longitudinal axis, leading to a height difference between inlet and outlet ports filled with cell culture medium. This simple method allows applying pressure gradients in a scalable, parallel manner. Applications of higher pressure values were leading to detachment of the hydrogel construct from the channel walls. In ongoing investigations, we aim to improve the hydrogel to chip adhesion by chemical surface modification and anchoring geometries.


4. Conclusion

Biofabrication with integrated cellular self-assembly is a powerful concept to decrease the fabrication demands, by increasing the tissue complexity intrinsically. We have shown that organ models with enhanced structural complexity and physiology compared to 2D monolayers can be fabricated from simplified cell patterns in hydrogels. With bioprinting, we gained control of self-assembly mechanisms, leading to scalable, size-defined and orientated epithelial cell spheroids and nephron-like tubules comprising a lumen, which are amenable to perfusion. This is a key step towards successful applications of 3D nephron models in screening applications, such as nephrotoxicity studies, where scalability of fabrication processes is a limiting factor. Current challenges of the presented concept are mainly related to the robustness of the resulting constructs. This included long-term mechanical stability of the hydrogel ECM itself, and stability of the chemical adhesion of the hydrogel to chip interface, which are under ongoing optimization.

Acknowledgments

We are grateful for excellent technical assistance by Amos Spielman, I Bierschenkand, S Haxelmans and the Life Imaging Center (LIC) in the Center for Bio-logical Systems Analysis (ZBSA) of the Albert-Ludwigs-University Freiburg for the excellent support in confocal microscopy image recording and analysis. This work was supported by the Baden-Württemberg Stiftung to SZ and SSL, the German Research Foundation (DFG) to SSL (Li 1817/2-1), the European Research Council to SSL (DiRECT), and the Swiss National Science Foundation to SSL (NCCR Kidney.CH). Furthermore, we thank the Baden Württemberg Stiftung for supporting this work with Grant No IAF-3.

ORCID iDs

Kevin Tröndle  <https://orcid.org/0000-0002-7699-3737>

Roman Pichler  <https://orcid.org/0000-0003-2602-998X>

References

- [1] Breslin S and O'Driscoll L 2013 Three-dimensional cell culture: the missing link in drug discovery *Drug Discovery Today* **18** 240–9
- [2] Langhans S A 2018 Three-dimensional *in vitro* cell culture models in drug discovery and drug repositioning *Front. Pharmacol.* **9** 6
- [3] Wilmer M J, Ng C P, Lanz H L, Vulto P, Suter-Dick L and Masereeuw R 2016 Kidney-on-a-chip technology for drug-induced nephrotoxicity screening *Trends Biotechnol.* **34** 156–70
- [4] Nieskens T T G and Wilmer M J 2016 Kidney-on-a-chip technology for renal proximal tubule tissue reconstruction *Eur. J. Pharmacol.* **790** 46–56
- [5] Huh D, Hamilton G A and Ingber D E 2011 From 3D cell culture to organs-on-chips *Trends Cell Biol.* **21** 745–54
- [6] Jang K-J and Suh K-Y 2010 A multi-layer microfluidic device for efficient culture and analysis of renal tubular cells *Lab Chip* **10** 36–42
- [7] Kaminski M M *et al* 2016 Direct reprogramming of fibroblasts into renal tubular epithelial cells by defined transcription factors *Nat. Cell Biol.* **18** 1269–80
- [8] Kang H M *et al* 2019 Effective reconstruction of functional organotypic kidney spheroid for *in vitro* nephrotoxicity studies *Sci. Rep.* **9** 17610
- [9] Buzhor E *et al* 2011 Kidney spheroids recapitulate tubular organoids leading to enhanced tubulogenic potency of human kidney-derived cells *Tissue Eng. A* **17** 2305–19
- [10] Secker P F, Luks L, Schlichenmaier N and Dietrich D R 2018 RPTEC/TERT1 cells form highly differentiated tubules when cultured in a 3D matrix *ALTEX* **35** 223–34
- [11] Hirashima T, Hoshuyama M and Adachi T 2017 *In vitro* tubulogenesis of Madin-Darby canine kidney (MDCK) spheroids occurs depending on constituent cell number and scaffold gel concentration *J. Theor. Biol.* **435** 110–5
- [12] DesRochers T M, Suter L, Roth A and Kaplan D L 2013 Bioengineered 3D human kidney tissue, a platform for the determination of nephrotoxicity *PLoS One* **8** e59219
- [13] Jakab K, Norotte C, Marga F, Murphy K, Vunjak-Novakovic G and Forgacs G 2010 Tissue engineering by self-assembly and bio-printing of living cells *Biofabrication* **2** 22001
- [14] Singh N K *et al* 2020 Three-dimensional cell-printing of advanced renal tubular tissue analogue *Biomaterials* **232** 119734
- [15] Homan K A *et al* 2016 Bioprinting of 3D convoluted renal proximal tubules on perfusable chips *Sci. Rep.* **6** 34845
- [16] Lin N Y C *et al* 2019 Renal reabsorption in 3D vascularized proximal tubule models *Proc. Natl Acad. Sci. USA* **116** 5399–404
- [17] Weber E J *et al* 2016 Development of a microphysiological model of human kidney proximal tubule function *Kidney Int.* **90** 627–37
- [18] Homan K A *et al* 2019 Flow-enhanced vascularization and maturation of kidney organoids *in vitro Nat. Methods* **16** 255–62
- [19] Morizane R, Lam A Q, Freedman B S, Kishi S, Valerius M T and Bonventre J V 2015 Nephron organoids derived from human pluripotent stem cells model kidney development and injury *Nat. Biotechnol.* **33** 1193–200

- [20] Freedman B S *et al* 2015 Modelling kidney disease with CRISPR-mutant kidney organoids derived from human pluripotent epiblast spheroids *Nat. Commun.* **6** 8715
- [21] Takasato M *et al* 2015 Kidney organoids from human iPS cells contain multiple lineages and model human nephrogenesis *Nature* **526** 564–8
- [22] Gutzweiler L *et al* 2017 Large scale production and controlled deposition of single HUVEC spheroids for bioprinting applications *Biofabrication* **9** 25027
- [23] Ayan B *et al* 2020 Aspiration-assisted bioprinting for precise positioning of biologics *Sci. Adv.* **6** eaaw5111
- [24] Tröndle K *et al* 2019 Bioprinting of high cell density constructs leads to controlled lumen formation with self-assembly of endothelial cells *J. Tissue Eng. Regen. Med.* **13** 1883–95
- [25] Brassard J A, Nikolaev M, Hübscher T, Hofer M and Lutolf M P 2020 Recapitulating macro-scale tissue self-organization through organoid bioprinting *Nat. Mater.* **20** 22–9
- [26] Bülow R D and Boor P 2019 Extracellular matrix in kidney fibrosis: more than just a scaffold *J. Histochem. Cytochem.* **67** 643–61
- [27] Morgan F L C, Moroni L and Baker M B 2020 Dynamic bioinks to advance bioprinting *Adv. Healthcare Mater.* **9** e1901798
- [28] Willerth S M, Arendas K J, Gottlieb D I and Sakiyama-Elbert S E 2006 Optimization of fibrin scaffolds for differentiation of murine embryonic stem cells into neural lineage cells *Biomaterials* **27** 5990–6003
- [29] Streule W, Lindemann T, Birkle G, Zengerle R and Koltay P 2004 PipeJet: a simple disposable dispenser for the nano- and microliter range *J. Assoc. Lab. Autom.* **9** 300–6
- [30] Khetan S and Burdick J 2009 Cellular encapsulation in 3D hydrogels for tissue engineering *J. Vis. Exp.* **32** 1–5
- [31] Afgan E *et al* 2016 The Galaxy platform for accessible, reproducible and collaborative biomedical analyses: 2016 update *Nucleic Acids Res.* **44** W1, W3–W10
- [32] Dobin A *et al* 2013 STAR: ultrafast universal RNA-seq aligner *Bioinformatics* **29** 15–21
- [33] Liao Y, Smyth G K and Shi W 2014 featureCounts: an efficient general purpose program for assigning sequence reads to genomic features *Bioinformatics* **30** 923–30
- [34] Love M I, Huber W and Anders S 2014 Moderated estimation of fold change and dispersion for RNA-seq data with DESeq2 *Genome Biol.* **15** 550
- [35] Shen Y *et al* 2012 A map of the cis-regulatory sequences in the mouse genome *Nature* **488** 116–20
- [36] Yu G, Wang L-G, Han Y and He Q-Y 2012 clusterProfiler: an R package for comparing biological themes among gene clusters *OMICS: J. Integr. Biol.* **16** 284–7
- [37] Wells E K, Yarborough O, Lifton R P, Cantley L G and Caplan M J 2013 Epithelial morphogenesis of MDCK cells in three-dimensional collagen culture is modulated by interleukin-8 *Am. J. Physiol., Cell Physiol.* **304** C966–75
- [38] Ng C P, Zhuang Y, Lin A W H and Teo J C M 2013 A fibrin-based tissue-engineered renal proximal tubule for bioartificial kidney devices: development, characterization and *in vitro* transport study *Int. J. Tissue Eng.* **2013** 1–10
- [39] Duong H, Wu B and Tawil B 2009 Modulation of 3D fibrin matrix stiffness by intrinsic fibrinogen–thrombin compositions and by extrinsic cellular activity *Tissue Eng. A* **15** 1865–76
- [40] Benning L *et al* 2017 Assessment of hydrogels for bioprinting of endothelial cells *J. Biomed. Mater. Res. A* **106** 935–47
- [41] Benning L *et al* 2017 Cytocompatibility testing of hydrogels toward bioprinting of mesenchymal stem cells *J. Biomed. Mater. Res. A* **105** 3231–41
- [42] Budday S, Ovaert T C, Holzapfel G A, Steinmann P and Kuhl E 2020 Fifty shades of brain: a review on the mechanical testing and modeling of brain tissue *Arch. Comput. Methods Eng.* **27** 1187–230
- [43] Guimarães C F, Gasperini L, Marques A P and Reis R L 2020 The stiffness of living tissues and its implications for tissue engineering *Nat. Rev. Mater.* **5** 351–70
- [44] Romagnani P, Lasagni L and Remuzzi G 2013 Renal progenitors: an evolutionary conserved strategy for kidney regeneration *Nat. Rev. Nephrol.* **9** 137–46
- [45] El-Sheikh A A K, Masereeuw R and Russel F G M 2008 Mechanisms of renal anionic drug transport *Eur. J. Pharmacol.* **585** 245–55
- [46] Nakano T *et al* 2019 Increased fibroblast growth factor-21 in chronic kidney disease is a trade-off between survival benefit and blood pressure dysregulation *Sci. Rep.* **9** 19247
- [47] Sasisekharan R, Ernst S and Venkataraman G 1997 On the regulation of fibroblast growth factor activity by heparin-like glycosaminoglycans *Angiogenesis* **1** 45–54
- [48] Gilmer G G, Deshpande V G, Chou C-L and Knepper M 2018 Flow resistance along the rat renal tubule *Am. J. Physiol. Renal Physiol.* **315** F1398–405